

Three dimensional V_2O_5/NaV_6O_{15} hierarchical heterostructures: Controlled synthesis and synergistic effect investigated by *in situ* X-ray diffraction

Chaojiang Niu^{a,1}, Xiong Liu^{a,1}, Jiashen Meng^{a,1}, Lin Xu^{b,*}, Mengyu Yan^a, Xuanpeng Wang^a, Guobin Zhang^a, Ziang Liu^a, Xiaoming Xu^a, Liqiang Mai^{a,*}

^a State Key Laboratory of Advanced Technology for Materials Synthesis and Processing, Wuhan University of Technology, Wuhan 430070, China

^b School of Chemical and Biomedical Engineering, Nanyang Technological University, 62 Nanyang Drive, Singapore 637459, Singapore

ARTICLE INFO

Article history:

Received 18 April 2016

Received in revised form

28 June 2016

Accepted 30 June 2016

Available online 30 June 2016

Keywords:

V_2O_5/NaV_6O_{15}

Hierarchical heterostructure

Controlled synthesis

Synergistic effect

In situ X-ray diffraction

ABSTRACT

Three-dimensional (3D) hierarchical heterostructures have been widely studied for energy storage because of their amazing synergistic effect. However, a detailed characterization how the branched structure affects the backbone structure during electrochemical cycling, and the specific relationship between the backbone and the branched heterogeneous structure (namely synergistic effect) have been rarely revealed. In addition, the controllable synthesis of this system still remains a great challenge. Herein, we developed a one-step gradient hydrothermal method to obtain a series of 3D hierarchical heterogeneous nanostructures, including V_2O_5/NaV_6O_{15} , V_2O_5/ZnV_2O_6 and V_2O_5/CoV_2O_6 , through controlling the sequence of nucleation and growth processes of different structural units in the same precursor. On the basis of time-resolved *in situ* X-ray diffraction (XRD) characterizations, we clearly elucidated the synergistic effect between the branched and backbone structure. During the synergistic effect, the branched NaV_6O_{15} helps to reduce the potential barrier during lithium-ion insertion/extraction, buffers the impact of crystal-system transformations during the charge/discharge process; the backbone V_2O_5 is beneficial to increase the charge/discharge capacity, inhibits the self-aggregation of branched NaV_6O_{15} and maintains the stability of 3D structure. Consequently, 3D V_2O_5/NaV_6O_{15} hierarchical heterogeneous microspheres exhibit the best electrochemical performance than pure V_2O_5 and V_2O_5/NaV_6O_{15} physical mixture in lithium-ion batteries (LIBs). When tested at a high rate of 5 A g^{-1} , 92% of the initial capacity can be maintained after 1000 cycles. We believe this method will be in favor of the construction of 3D hierarchical heterostructures and this specific synergistic effect investigated by *in situ* XRD will be significant for the design of better electrodes.

© 2016 Elsevier Ltd. All rights reserved.

1. Introduction

Three-dimensional (3D) hierarchical heterogeneous nanostructures, benefiting from the synergistic effect, a robust structure and a large number of active sites, have been widely studied and applied in the fields of optics, catalysis and energy storage [1–14]. Zhou et al. have synthesized 3D branched Fe_2O_3/SnO_2 heterostructure by combining vapor transport deposition and hydrothermal growth methods to effectively improve the electrochemical performance of lithium-ion batteries (LIBs) via a synergistic effect [15]. Mai et al. have obtained 3D $MnMoO_4/CoMoO_4$ hierarchical heterostructured nanowires through a microemulsion and refluxing

method, which exhibited superior supercapacitor performance to single molybdate or their physical mixture [16]. However, a detailed characterization how the branched nanostructure affects the backbone structure during electrochemical cycling, and an in-depth understanding of the relationship between the backbone structure and the branched heterogeneous nanostructure, namely synergistic effect, have been rarely revealed [17–26].

Hydrothermal synthesis provides a simple and controllable bottom-up approach for fabricating various nanostructures, including 0D, 1D, 2D and 3D nanostructures. Its advantages are confirmed as energy conservation, high yields and convenient process [27–33]. To obtain a uniform morphology for a single substance, the nucleation and growth process of both homogeneous and heterogeneous types are usually separated into two distinct steps. Many efforts have focused on precisely controlling the synthetic conditions of different steps to obtain different homogeneous nanostructures [34–39]. However, the fabrication of 3D hierarchical

* Corresponding author.

E-mail addresses: xu.lin@ntu.edu.sg (L. Xu), mlq518@whut.edu.cn (L. Mai).

¹ These authors contributed equally to this work.

heterostructures usually contains more than two different substances. The nucleation and growth stages of the various substances in one system will become complicated and chaotic, leading to nonuniform nanostructure mixtures. And few reports have successfully realized these efficient separation in one system to obtain uniform 3D hierarchical heterostructures [40,41].

Vanadium pentoxide (V_2O_5), which exhibits high capacity, is expensive and derived from an abundant source. This compound has been widely studied as a cathode material in LIBs [42–45]. However, its poor rate capability and low cycling stability seriously limit its further application in energy storage field [46–48]. Nevertheless, many vanadates, such as NaV_6O_{15} , ZnV_2O_6 and CoV_2O_6 , exhibit much stable cycling performance when used as LIB electrodes, yet they have relatively low discharge capacities [49–51]. Therefore, how to design and fabricate these heterogeneous materials with synergistic effect to combine the advantages of both high capacity and stable cycling performance is important and challenging.

Herein, we report a one-step gradient hydrothermal method to synthesize a series of 3D hierarchical heterostructures, including V_2O_5/NaV_6O_{15} , V_2O_5/ZnV_2O_6 and V_2O_5/CoV_2O_6 . This method is based on different nucleation rates of two substances, realizing the sequence of nucleation and growth of different structural units derived from a single precursor. The backbone vanadium oxide nanogears are first formed using a solution with one concentration of reactants, subsequently, the branched sodium vanadate nanospindles are obtained and matched up to the backbone in the same precursor. Using time-resolved *in situ* X-ray diffraction (XRD), we clearly elucidate the synergistic effect between the branched vanadate (NaV_6O_{15}) and the backbone structure (V_2O_5) during the charge/discharge process. Therefore, 3D V_2O_5/NaV_6O_{15} hierarchical heterogeneous microsphere cathode can exhibit better electrochemical performance in LIBs than pure V_2O_5 , NaV_6O_{15} and V_2O_5/NaV_6O_{15} physical mixture.

2. Material and methods

2.1. Preparation of hierarchical V_2O_5 microspheres

NH_4VO_3 and $C_6H_8O_7 \cdot H_2O$ were added to 35 mL of H_2O and stirred for 24 h at 50 °C until a homogeneous blue solution was obtained. This solution was subsequently transferred to a 50 mL Teflon autoclave and maintained at 180 °C for 24 h. After the solution was cooled to room temperature, black powders were obtained by gently washing and drying in air at 70 °C for 12 h. The final products were obtained after sintering in air at 450 °C (2 °C min^{-1}) for 5 h.

2.2. Preparation of NaV_6O_{15} nanospindles

0.364 g of V_2O_5 was dispersed in 30 mL of distilled water, 5 mL of 30% H_2O_2 and 1.5 g of NaCl were added under vigorous magnetic stirring at room temperature. The mixture was maintained for 2 h until an orange suspension solution was obtained. Then transferred to a 40 mL autoclave and heated in an oven at 200 °C for 4 days. The final products were obtained after washing, drying and sintering in air at 450 °C (2 °C min^{-1}) for 5 h.

2.3. Preparation of 3D V_2O_5/NaV_6O_{15} hierarchical heterogeneous microspheres

NH_4VO_3 , $C_6H_8O_7 \cdot H_2O$ and $C_{12}H_{25}SO_4Na$ were added to 35 mL of H_2O and then stirred for 24 h at 50 °C until a homogeneous blue solution was obtained. Then transferred to a 50 mL Teflon autoclave and maintained at 180 °C for 24 h. After cooling to room temperature, black powders were obtained by gently washing and drying in air at 70 °C for 12 h. The final products were successfully synthesized after being sintered in air at 450 °C (2 °C min^{-1}) for 5 h.

2.4. Preparation of V_2O_5/NaV_6O_{15} physical mixture

The V_2O_5/NaV_6O_{15} physical mixture is prepared by mixing NaV_6O_{15} nanospindles and V_2O_5 microspheres, and the weight ratio of NaV_6O_{15} and V_2O_5 is 1:2 in the physical mixture, which is similar in 3D V_2O_5/NaV_6O_{15} hierarchical heterogeneous microspheres (1:1.96).

2.5. Preparation of 3D V_2O_5/ZnV_2O_6 hierarchical heterogeneous microspheres

NH_4VO_3 , $C_6H_8O_7 \cdot H_2O$ and $Zn(CH_3COO)_2 \cdot 2H_2O$ were added to 8 mL of H_2O and stirred for 4 h at 50 °C until a homogeneous blue solution was obtained. Then transferred to a 15 mL Teflon autoclave and maintained at 180 °C for 15 h. After the solution cooled to room temperature, black powders were obtained by gently washing and drying in air at 70 °C for 12 h. The final products were obtained after sintering in air at 450 °C (2 °C min^{-1}) for 5 h.

2.6. Preparation of 3D V_2O_5/CoV_2O_6 hierarchical heterogeneous microspheres

NH_4VO_3 , $C_6H_8O_7 \cdot H_2O$ and $Co(CH_3COO)_2 \cdot 4H_2O$ were added to 8 mL of H_2O and stirred for 4 h at 50 °C until a homogeneous blue solution was obtained. Then transferred to a 15 mL Teflon autoclave and maintained at 180 °C for 24 h. After cooling to room temperature, black powders were obtained by gently washing and drying in air at 70 °C for 12 h. The final products were successfully synthesized after sintering in air at 450 °C (2 °C min^{-1}) for 5 h.

3. Characterization

The crystallographic information of the final products was measured using a Bruker D8 Discover X-ray diffractometer equipped with a Cu-K α radiation source; the samples were scanned over a 2 θ range from 10° to 80° at room temperature. Scanning electron microscope (SEM) images were collected using a JEOL-7100 F SEM. Transmission electron microscope (TEM) images were collected using a JEM-2100 F TEM. The Brunauer-Emmett-Teller (BET) specific surface area was calculated from nitrogen adsorption isotherms measured at 77 K using a Tristar-3020 instrument. Energy-dispersive X-ray spectra (EDS) were recorded using an Oxford IE250 system. UV–VIS spectra were obtained using a UV/VIS/NIR Spectrometer (PerkinElmer, Lambda 750 S).

Type 2016 coin cells were assembled in a glovebox filled with pure argon gas. Lithium foil was used as the anode and a solution of $LiPF_6$ (1 M) in EC/DEC (1:1 vol/vol) was used as the electrolyte. The cathode was composed of a ground mixture of 70% active material, 20% acetylene black and 10% poly(tetrafluoroethylene). Galvanostatic charge/discharge measurements were performed using a multichannel battery testing system (LAND CT2001A). Cyclic voltammograms (CV) and electrochemical impedance spectra (EIS) were collected using an Autolab potentiostat/galvanostat. For *in situ* XRD measurement, the electrode was placed right behind an X-ray-transparent beryllium window which is also acted as a current collector. The *in situ* XRD signals were collected using the planar detector in a still mode during the discharge-charge process, and each pattern took 2 min to acquire.

4. Results and discussion

The formation process of 3D V_2O_5/NaV_6O_{15} hierarchical heterogeneous microspheres (noted as 3D microspheres) via a one-step gradient hydrothermal method was studied with a series of experiments (Fig. 1). The corresponding low-magnification SEM

images show the overall morphologies (Fig. S1). During the initial stage (Fig. 1a, e), cross V_2O_5 nanosheets are firstly obtained via reaction for 2 h because of the abundant vanadium source and fast nucleation and grown rate [42,48]. When the reaction time is increased to 6 h (Fig. 1b, f), consistent with the lowest energy principle [31,32,35,40], more and more fresh half V_2O_5 nanosheets continuously grow at the junction of former cross nanosheets, forming V_2O_5 nanogears composed of rectangular nanosheets (~ 100 nm in thickness, $\sim 4 \mu\text{m}$ in length and $\sim 2 \mu\text{m}$ in width). As shown in the SEM images of pure V_2O_5 nanogears (Fig. 2a, b), only two nanosheets cross over at the center, whereas the other half nanosheets grow from their intersection. With a further increase in reaction time, sodium vanadate nanospindles begin to form and preferentially grow on the edges of the vanadium oxide nanosheets through heterogeneous nucleation (Fig. 1c,g). Then, the sodium vanadate nanospindles grow larger and denser, homogeneously covering the whole surface of the vanadium oxide nanogears (Figs. 1d,h and 2c-e), which is also evidenced by the EDS mapping (Fig. S2). The mass ratio between NaV_6O_{15} and V_2O_5 in 3D V_2O_5/NaV_6O_{15} hierarchical heterogeneous microspheres is $\sim 1:1.96$ (Fig. S2e). Eventually, 3D V_2O_5/NaV_6O_{15} hierarchical heterogeneous microspheres are obtained after proper calcination. The corresponding SEM image and XRD pattern clearly demonstrate the morphology and structural phase of each stage (Fig. 1). As shown in the TEM images, the (101) interlayer spacing of the V_2O_5 nanosheets is 0.44 nm (measured at the nanosheets edge), close to the 0.47 nm (200) interlayer spacing of NaV_6O_{15} nanospindles (Fig. 2g, h). Therefore, the NaV_6O_{15} nanospindles can directly fit into the V_2O_5 nanosheets and continue to grow, forming stable hierarchical heterostructure. The corresponding SAED pattern exhibits well crystallinity (inset of Fig. 2h). When the reaction time is extended to 48 h, the hierarchical NaV_6O_{15} nanospindles become swollen (Fig. S3).

To explore the specific influence of the sodium source, we conducted a series of control experiments by varying the quantity of $C_{12}H_{25}SO_4Na$ (sodium dodecyl sulfate, SDS) from 0 to 0.1, 0.3, 0.5 and 1.5 g (Figs. S4 and S5). Only pure V_2O_5 nanogears are obtained in the absence of SDS. After a small amount of SDS (0.1 g) is added, small NaV_6O_{15} nanospindles emerge mostly on the edges of V_2O_5 nanosheets. With an increasing amount of SDS, larger NaV_6O_{15} nanospindles appear and gradually cover the whole surface of the V_2O_5 nanogears, forming 3D V_2O_5/NaV_6O_{15} hierarchical heterogeneous microspheres. When an excess amount of SDS (1.5 g) is added, only pure NaV_6O_{15} is obtained (Fig. S5). Furthermore, 3D microspheres were also synthesized when SDS was replaced with another sodium source, sodium dodecyl benzene sulfonate ($C_{18}H_{29}NaO_3S$), demonstrating the substitutability of the sodium source (Fig. S6).

On the basis of the afore-mentioned experiments, a one-step gradient hydrothermal method is proposed to further clarify the formation mechanism of 3D hierarchical heterostructures (Fig. S7). The complicated process can be divided into two parts according to the different nucleation and growth rates of different materials. The first part is the nucleation and growth of vanadium oxide, denoted as VO (Fig. S7), with a low nucleation energy barrier and a fast growth rate. The second part is the nucleation and growth of the vanadates, denoted as M-VO, with a high nucleation energy barrier and a slow growth rate. Because the formation of M-VO requires higher energy and longer time than the formation of VO when they are synthesized under the same conditions (Figs. 1, S4 and S5). Taking the formation process of 3D V_2O_5/NaV_6O_{15} hierarchical heterogeneous microspheres as an example, the precursor solution initially contains two monomers: an abundant of vanadium source and a small amount of sodium source. The solution firstly reaches supersaturation of vanadium oxide, owing to the low nucleation energy barrier and abundant source, vanadium oxide nucleates homogeneously, grows into

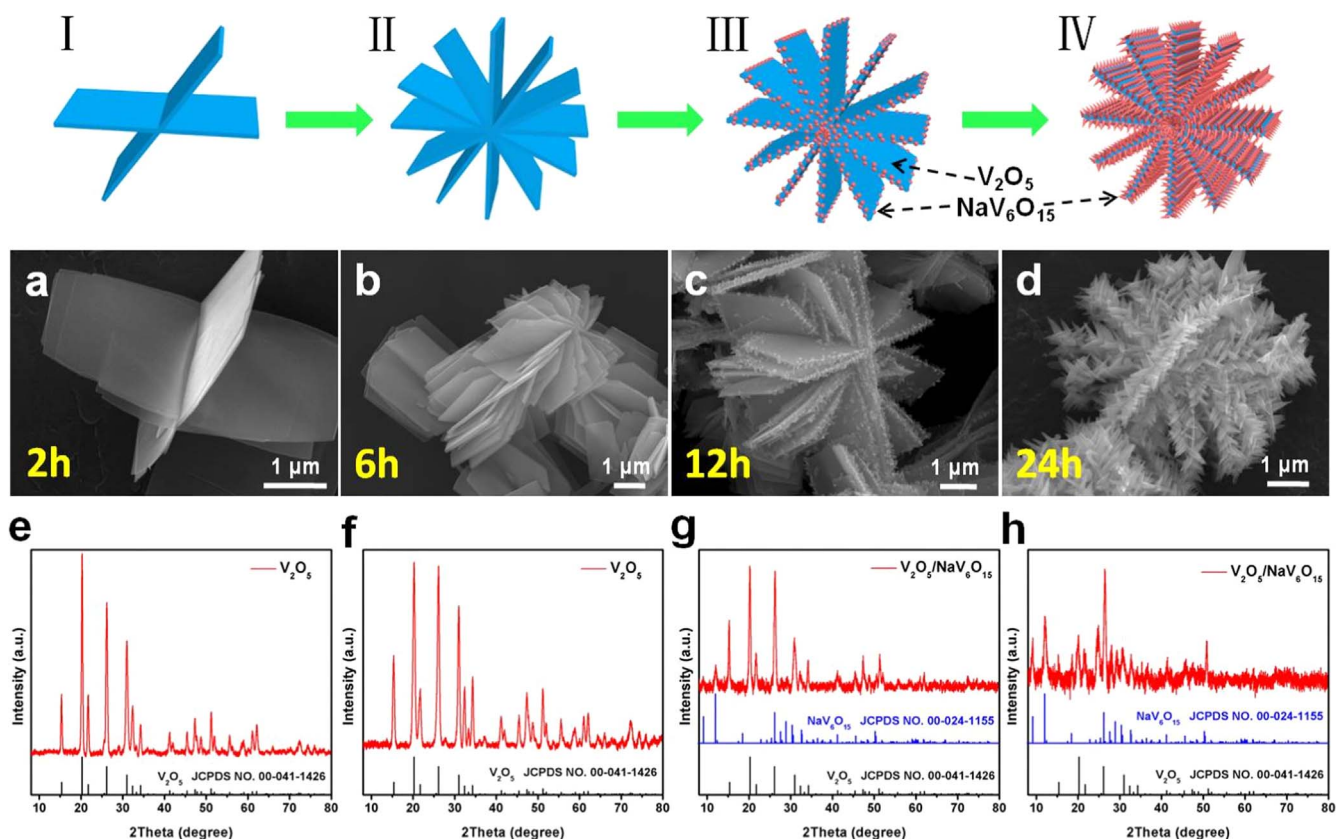


Fig. 1. Schematic of the formation process of 3D V_2O_5/NaV_6O_{15} hierarchical heterogeneous microspheres through a one-step gradient hydrothermal method. SEM images (a-d) of samples prepared at 2, 6, 12 and 24 h, the corresponding XRD patterns (e-h) after annealing in air for 5 h at 450 °C.

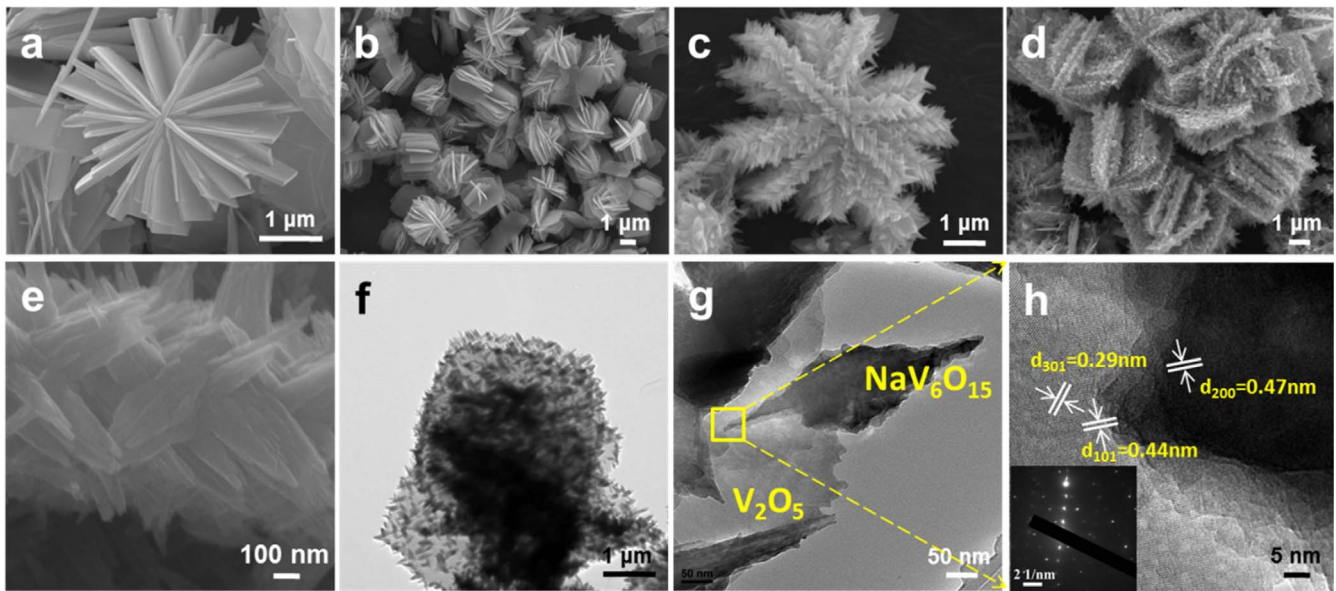


Fig. 2. (a–b) SEM images of V_2O_5 nanogears. SEM images (c–e), TEM images (f–g), high resolution TEM image (h) and SAED pattern (inset of h) of 3D V_2O_5/NaV_6O_{15} hierarchical heterogeneous microspheres.

nanosheets and forms nanogears. This process results in a decrease of the vanadium monomer concentration. Then sodium vanadate reaches the supersaturation level, heterogeneously nucleates and grows into nanospindles on the edge of vanadium oxide nanogears. Therefore, the nucleation and growth processes of vanadium oxide and sodium vanadate are efficiently separate and occur sequentially. After sintering in air, 3D V_2O_5/NaV_6O_{15} hierarchical heterogeneous microspheres are obtained (Table S1).

To confirm the generality of this one-step gradient hydrothermal method, 3D V_2O_5/ZnV_2O_6 and V_2O_5/CoV_2O_6 hierarchical heterostructures were also synthesized on the basis of this mechanism (Fig. 3). The corresponding low-magnification SEM images show the overall morphologies (Fig. S8). The XRD patterns of their precursors for V_2O_5/NaV_6O_{15} , V_2O_5/ZnV_2O_6 and V_2O_5/CoV_2O_6 heterogeneous microspheres have also been characterized (Fig. S9). Similar to the formation process of 3D V_2O_5/NaV_6O_{15} hierarchical heterogeneous microspheres, pure V_2O_5 microspheres,

which are made up of small nanosheets, are first obtained in accordance with the curve of VO. Then, fresh ZnV_2O_6 and CoV_2O_6 nanoparticles nucleate on the edge and surface of V_2O_5 microspheres, respectively, in accordance with the curve of M–VO. Eventually, 3D V_2O_5/ZnV_2O_6 and V_2O_5/CoV_2O_6 hierarchical heterogeneous microspheres are obtained (Figs. S10, and S11), demonstrating the universality of this feasible method.

The CV curves of 3D V_2O_5/NaV_6O_{15} hierarchical heterogeneous microspheres, pure V_2O_5 nanogears, NaV_6O_{15} nanospindles were obtained to characterize the phase transformation and ionic diffusion process that occurs during the reaction when measured in 2.4–4.0 V at a scan rate of 0.1 mV s^{-1} (Figs. 4a–c, S12). 3D microspheres exhibit six pairs of peaks, three pairs of peaks on the two sides (2.67/2.53 V, 2.95/2.90 V, 3.75/3.61 V) are associated with NaV_6O_{15} , while the middle two pairs of peaks (3.25/3.17 V, 3.45/3.38 V) belong to V_2O_5 [45,46]. This indicates that the lithium ions first diffuse into the outer branched NaV_6O_{15} nanospindles and then intercalate into the V_2O_5

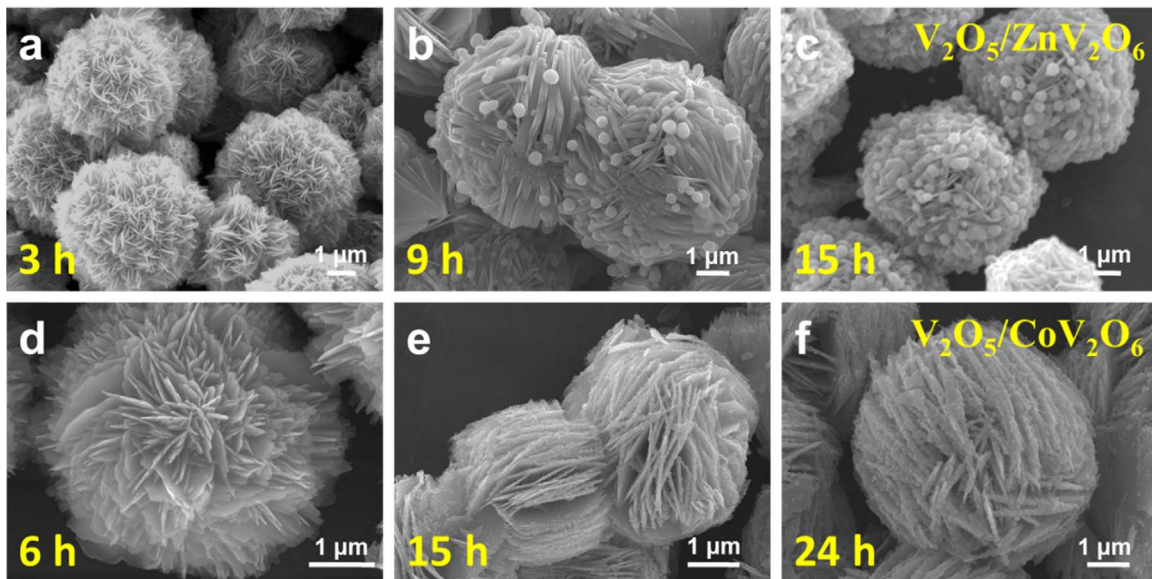


Fig. 3. The extension of gradient hydrothermal method. (a–c) SEM images of 3D V_2O_5/ZnV_2O_6 hierarchical heterogeneous microspheres prepared at 3, 9 and 15 h, respectively. (d–f) SEM images of 3D V_2O_5/CoV_2O_6 hierarchical heterogeneous microspheres prepared at 6, 15 and 24 h, respectively.

backbone during the discharge process. Another pair of peaks (3.27/3.30 V) is also attributable to $\text{NaV}_6\text{O}_{15}$. The middle V_2O_5 peaks of the 3D structure exhibit a lower overpotential (80 and 70 mV) than those (160 and 110 mV) of pure V_2O_5 nanogears, indicating smaller polarization during the lithium-ion insertion and extraction processes. Compared with pure V_2O_5 nanogears and $\text{V}_2\text{O}_5/\text{NaV}_6\text{O}_{15}$ physical mixture, 3D microspheres exhibit better rate capability and cycling performance; they recover 97% of their initial capacity after being tested at various rates of 100, 200, 500, 1000, 2000, 5000 and again at 100 mA g^{-1} (Fig. 4d). However, the pure V_2O_5 nanogears and $\text{V}_2\text{O}_5/\text{NaV}_6\text{O}_{15}$ physical mixture recover only 85% and 67% of their initial capacities, respectively. After cycling 200 times at 2000 mA g^{-1} , the discharge capacities of V_2O_5 nanogears and $\text{V}_2\text{O}_5/\text{NaV}_6\text{O}_{15}$ physical mixture fade obviously, with capacity retentions of 75% and 67%, respectively. Their retention rates are much lower than that of 3D microspheres (98%) (Fig. 4e). When tested at a low rate of 500 mA g^{-1} , 3D microspheres remain a discharge capacity of 112 mA h g^{-1} after cycling 200 times, corresponding to a capacity retention of 100% and the coulombic efficiency is close to 100%. Notably, even when measured at a high rate of 5000 mA g^{-1} ,

3D microspheres remain stable for 1000 cycles, with a capacity retention of 92% and a capacity fading of 0.0083% per cycle (Fig. 4h), demonstrating outstanding high-rate and long-term cycling performance. For 3D $\text{V}_2\text{O}_5/\text{ZnV}_2\text{O}_6$ and $\text{V}_2\text{O}_5/\text{CoV}_2\text{O}_6$ hierarchical heterogeneous microspheres, CV measurements were carried out to characterize the electrochemical reactions in 2.4–4.0 V at a scan rate of 0.2 mV s^{-1} (Fig. S13). In both $\text{V}_2\text{O}_5/\text{ZnV}_2\text{O}_6$ and $\text{V}_2\text{O}_5/\text{CoV}_2\text{O}_6$ hierarchical heterogeneous microspheres, two pairs of peaks belong to V_2O_5 , demonstrating that ZnV_2O_6 and CoV_2O_6 contribute little in the electrochemical performance of $\text{V}_2\text{O}_5/\text{ZnV}_2\text{O}_6$ and $\text{V}_2\text{O}_5/\text{CoV}_2\text{O}_6$.

As previously discussed, 3D hierarchical heterostructure produces a synergistic effect during the lithium-ion insertion/extraction and can improve the overall electrochemical performance [19–23,52,53]. To clearly reveal this synergistic effect inherent to 3D hierarchical heterostructure, we characterized the structural evolutions of 3D $\text{V}_2\text{O}_5/\text{NaV}_6\text{O}_{15}$ hierarchical heterogeneous microspheres, $\text{V}_2\text{O}_5/\text{NaV}_6\text{O}_{15}$ physical mixture, pure V_2O_5 nanogears and pure $\text{NaV}_6\text{O}_{15}$ nanospindles by *in situ* XRD during lithium-ion insertion and extraction process (Fig. 5). The clean and high-quality XRD patterns were obtained during the original cycles of galvanostatic

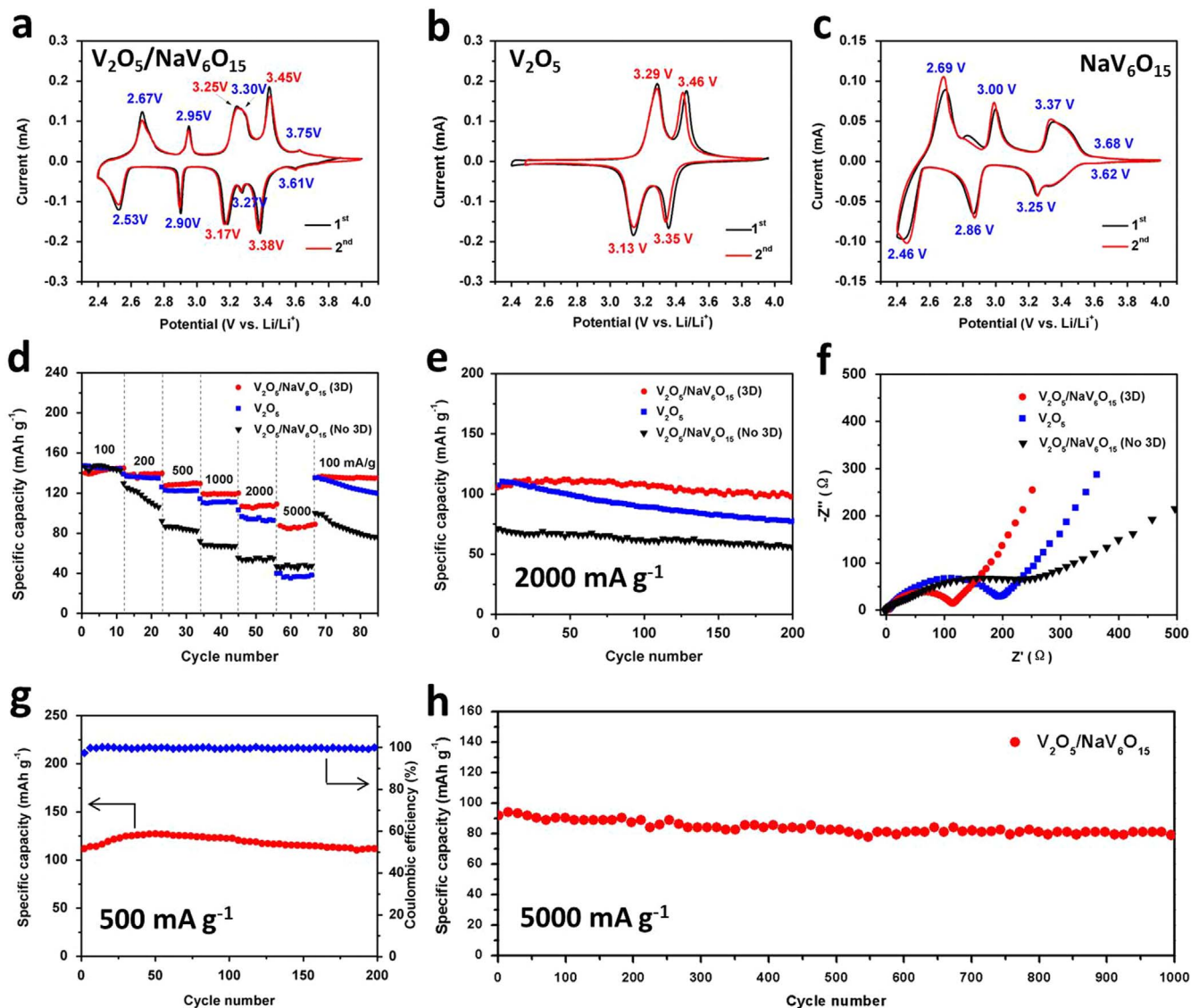


Fig. 4. (a–c) CV curves of 3D $\text{V}_2\text{O}_5/\text{NaV}_6\text{O}_{15}$ hierarchical heterogeneous microspheres (a), V_2O_5 nanogears (b) and $\text{NaV}_6\text{O}_{15}$ nanospindles (c) tested over 2.4–4 V at a scan rate of 0.1 mV s^{-1} . (d–f) Rate performance (d), cycling performance (e) and AC-impedance spectra (f) of 3D $\text{V}_2\text{O}_5/\text{NaV}_6\text{O}_{15}$ hierarchical heterogeneous microspheres, V_2O_5 nanogears and $\text{V}_2\text{O}_5/\text{NaV}_6\text{O}_{15}$ physical mixture. (g) Cycling performance and Coulombic efficiency of 3D $\text{V}_2\text{O}_5/\text{NaV}_6\text{O}_{15}$ hierarchical heterogeneous microspheres tested at 500 mA g^{-1} . (h) Long cycling performance of 3D $\text{V}_2\text{O}_5/\text{NaV}_6\text{O}_{15}$ hierarchical heterogeneous microspheres tested at a high rate of 5000 mA g^{-1} .

charge and discharge at a current density of 50 mA g^{-1} . An appreciable variation of the positive region within a 2θ range of $12\text{--}34^\circ$ was observed, indicating the existence and phase transition with different lattice parameters during the charge and discharge process.

These *in situ* XRD patterns exhibit three main characteristics (Fig. 5a–d). First, the (001) and (101) reflection peaks of V_2O_5 shift and recover repeatedly during the charge and discharge processes (Fig. 5c). The corresponding selected individual diffraction patterns were also provided to confirm the fully recovery of the structure (Fig. S14). When the lithium ions are inserted into the V_2O_5 along these directions, the corresponding peaks shift toward lower angles. When the lithium ions are extracted, the peaks return to their original positions, corresponding to the main conventional steps of lithium storage. However, the XRD patterns of 3D microspheres exhibit distinct plateaus during lithiation/delithiation (Fig. 5a). These plateaus do not appear in the profiles of the $\text{V}_2\text{O}_5/\text{NaV}_6\text{O}_{15}$ physical mixture or those of the pure $\text{NaV}_6\text{O}_{15}$ nanospindles (Fig. 5b, d). Second, the (300) reflection peak of $\text{NaV}_6\text{O}_{15}$ fluctuates in the XRD patterns of 3D microspheres, but it shifts slightly and tends toward a straight line in the pattern of pure $\text{NaV}_6\text{O}_{15}$ nanospindles and $\text{V}_2\text{O}_5/\text{NaV}_6\text{O}_{15}$ physical mixture. Third, the patterns of both pure $\text{NaV}_6\text{O}_{15}$ nanospindles and 3D microspheres show a stable reflection peak at 17.8° . However, the corresponding peak of the $\text{V}_2\text{O}_5/\text{NaV}_6\text{O}_{15}$ physical mixture exhibits an obvious intermittent phenomenon. This instability may be attributed to the junction of V_2O_5 and $\text{NaV}_6\text{O}_{15}$, which strengthens the solid solution and weakens changes in the lattice caused by phase transformations. The first two characteristics demonstrate that the 3D hierarchical heterostructure can effectively improve the reaction kinetics and increase the transport efficiency of lithium ions during the charge and discharge processes.

To further reveal these features, we elucidated the time-resolved phase evolution for the second discharge process of the 3D $\text{V}_2\text{O}_5/\text{NaV}_6\text{O}_{15}$ hierarchical heterogeneous microspheres by combining *in situ* XRD, the corresponding discharge curves and XRD Rietveld refinements (Figs. 5e–g, S15–S21). During the discharge process, six stages of phase transformations are observed and exhibited accurately with increasing time (Table 1). At the beginning of the constant-current reduction process from 0 to 410 s (stage I), the second discharge process starts at 20,801 s, and the discharge current density is constant at 50 mA g^{-1} , no obvious peak evolution occurs (Figs. S15 and S16). Only a slight phase transformation is evident between $\text{Na}_{1/3}\text{V}_2\text{O}_5$ and $\text{Li}_{1/18}\text{Na}_{1/3}\text{V}_2\text{O}_5$, without a change of the crystal system. This transformation leads to a tiny increase in the length of the *c*-axis in the unit cell of $\text{Na}_{1/3}\text{V}_2\text{O}_5$. As the discharge time increases from 410 to 1665 s (stage II), the evolution of a distinct peak associated with V_2O_5 occurs. This peak evolution indicates a phase transformation from V_2O_5 to $\epsilon\text{-Li}_{0.5}\text{V}_2\text{O}_5$. The crystal structure of V_2O_5 correspondingly changes from orthorhombic to a monoclinic phase with an increase of the length of the *c*-axis in the V_2O_5 unit cell (Figs. S16 and S17). From 1665 to 2500 s (stage III), the $\text{Li}_{1/18}\text{Na}_{1/3}\text{V}_2\text{O}_5$ phase transforms to $\text{Li}_{1/6}\text{Na}_{1/3}\text{V}_2\text{O}_5$, corresponding to no variation of the crystal system, but resulting in a slight increase of the lattice parameters for $\text{Na}_{1/3}\text{V}_2\text{O}_5$ (Figs. S17 and S18). With the sequential discharge process from 2500 to 3745 s (stage IV), another peak evolution of V_2O_5 is evidenced, which reveals the phase transformation from $\epsilon\text{-Li}_{0.5}\text{V}_2\text{O}_5$ to $\delta\text{-LiV}_2\text{O}_5$ and the crystal-structure phase transition from monoclinic to orthorhombic. However, the structure of $\text{Li}_{1/6}\text{Na}_{1/3}\text{V}_2\text{O}_5$ remains stable (Figs. S18 and S19). When the discharge time reaches 5000 s (stage V), an evolution of $\text{Na}_{1/3}\text{V}_2\text{O}_5$ is observed, indicating the phase transformation from $\text{Li}_{1/6}\text{Na}_{1/3}\text{V}_2\text{O}_5$ to $\text{Li}_{1/3}\text{Na}_{1/3}\text{V}_2\text{O}_5$ with an expansion of the lattice. However, the structure of $\delta\text{-LiV}_2\text{O}_5$ remains unchanged (Figs. S19 and S20). During the final stage from 5000 to 10,000 s (stage VI), only the evolution of $\text{Na}_{1/3}\text{V}_2\text{O}_5$ occurs, which results in a new phase of $\text{LiNa}_{1/3}\text{V}_2\text{O}_5$ and large changes in the

lattice parameters (Figs. S20 and S21).

These evidences clearly demonstrate a synergistic effect between the branched $\text{NaV}_6\text{O}_{15}$ and V_2O_5 backbone of the 3D $\text{V}_2\text{O}_5/\text{NaV}_6\text{O}_{15}$ hierarchical heterogeneous microspheres during the lithium-ion insertion/extraction, which can efficiently enhance the electrochemical performance. First, the branched $\text{NaV}_6\text{O}_{15}$ effectively reduces the potential barrier associated with lithium-ion insertion/extraction and increases the ionic conductivity. Test results, *i.e.*, CV (Fig. 4a–c) and *in situ* XRD (Fig. 5), demonstrate that lithium ions initially penetrate the outer branched $\text{NaV}_6\text{O}_{15}$ nanospindles and then insert into the V_2O_5 backbone during the discharge process. 3D microspheres exhibit a small charge transfer resistance of 110Ω (Fig. 4f), much lower than pure V_2O_5 nanogears and $\text{V}_2\text{O}_5/\text{NaV}_6\text{O}_{15}$ physical mixture (196Ω and 390Ω), showing faster ion mobility. To assess the lithium-ion diffusion kinetics of different electrodes, the calculations based on the impedance data in low frequency region were carried out (Fig. S22). Obviously, 3D $\text{V}_2\text{O}_5/\text{NaV}_6\text{O}_{15}$ hierarchical heterogeneous microspheres exhibit the lowest slope value ($k_1=14.3$) compared with pure V_2O_5 nanogears ($k_2=21.6$) and $\text{V}_2\text{O}_5/\text{NaV}_6\text{O}_{15}$ physical mixture ($k_3=71.3$). The corresponding diffusion coefficient values of lithium-ion are 2.8×10^{-7} , 1.3×10^{-7} and $1.1 \times 10^{-8} \text{ cm}^2 \text{ s}^{-1}$, respectively. The open circuit potentials for the EIS measurement (Fig. 4f) are 3.68, 3.55 and 3.62 V, respectively. And the EIS under different depth of 3D $\text{V}_2\text{O}_5/\text{NaV}_6\text{O}_{15}$ hierarchical heterogeneous microspheres during the discharge process are also performed to characterize the electrochemical reactions under different potentials (Fig. S23). The EIS curves from 3.68 V to 3.21 V during the V_2O_5 discharge process have two semicircles, the corresponding R_{ct} values are much smaller than that at 3.00 V. Moreover, the band gap value of $\text{NaV}_6\text{O}_{15}$ is 1.6 eV, smaller than that of V_2O_5 (2.2 eV), which is also beneficial to facilitate electronic diffusion (Fig. S24) [54,55]. Second, the branched $\text{NaV}_6\text{O}_{15}$ can greatly buffer the impact of crystal-system transformations during the charge and discharge process, thereby reducing the stress caused by lithium-ion insertion and extraction, thus decreasing the polarization of the electrodes. The $\text{NaV}_6\text{O}_{15}$ features have $(\text{V}_2\text{O}_5)_x$ -framework tunnels along their *b* axis and the sodium ions are aligned in these tunnels, which exhibits a crystal structure similar to that of V_2O_5 , with good lattice matching. This similarity is also confirmed in the high-resolution TEM image (Fig. 2h), where the (200) interlayer space of $\text{NaV}_6\text{O}_{15}$ is 0.47 nm and the (101) interlayer space of V_2O_5 is 0.44 nm. During all six stages, the monoclinic structure is kept stable throughout the charge and discharge processes (Table 1). Third, the backbone V_2O_5 is beneficial to increase the charge and discharge capacity of 3D microspheres, inhibits the self-aggregation of branched $\text{NaV}_6\text{O}_{15}$ and maintains the stability of 3D hierarchical heterogeneous structure. Compared with pure V_2O_5 nanogears and $\text{V}_2\text{O}_5/\text{NaV}_6\text{O}_{15}$ physical mixture, 3D microspheres exhibit the highest discharge capacity at each current density (Fig. 4d, e). After cycling 50 times at the current density of 500 mA g^{-1} , the 3D microspheres structural integrity are kept very well, while pure V_2O_5 nanogears are broken and aggregate together (Fig. S25). And 3D microspheres exhibit a higher specific surface area ($22 \text{ m}^2 \text{ g}^{-1}$) than that of V_2O_5 nanogears ($14 \text{ m}^2 \text{ g}^{-1}$). Consequently, this synergistic effect can greatly improve the electrochemical performance of 3D $\text{V}_2\text{O}_5/\text{NaV}_6\text{O}_{15}$ hierarchical heterogeneous microspheres.

5. Conclusions

Uniform 3D hierarchical heterogeneous microspheres ($\text{V}_2\text{O}_5/\text{NaV}_6\text{O}_{15}$, $\text{V}_2\text{O}_5/\text{ZnV}_2\text{O}_6$ and $\text{V}_2\text{O}_5/\text{CoV}_2\text{O}_6$) were synthesized by a one-pot gradient hydrothermal method. This strategy was realized by controlling the sequence of nucleation and growth stages for different substances in the same precursor. This technique

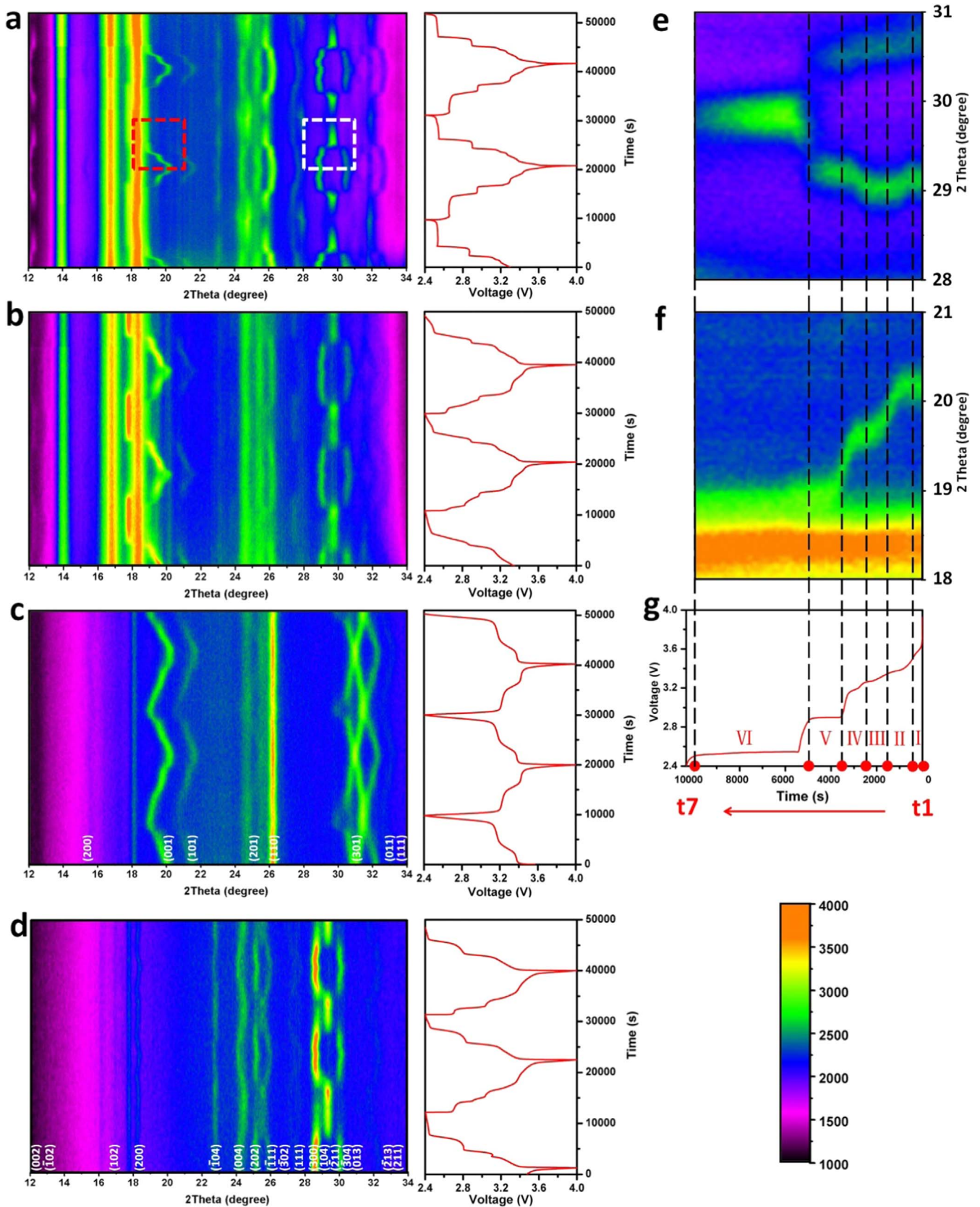


Fig. 5. *In situ* X-ray diffraction patterns of 3D $\text{V}_2\text{O}_5/\text{NaV}_6\text{O}_{15}$ hierarchical heterogeneous microspheres (a), $\text{V}_2\text{O}_5/\text{NaV}_6\text{O}_{15}$ physical mixture (b), pure V_2O_5 nanogears (c) and pure $\text{NaV}_6\text{O}_{15}$ nanospindles (d), during galvanostatic charge and discharge at 50 mA g^{-1} . The horizontal axis represents the selected 2θ regions from $12\text{--}34^\circ$, and time is plotted on the vertical axis. The corresponding voltage curve is plotted to the right. The diffraction intensity is color coded according to the scale bar in the bottom right corner. (e–g) Magnified time-resolved evolution of 3D $\text{V}_2\text{O}_5/\text{NaV}_6\text{O}_{15}$ hierarchical heterogeneous microspheres in one discharge process from 4.0 to 2.4 V. (e) *In situ* X-ray diffraction patterns selected from 28° to 31° in the white box of (a). (f) *In situ* X-ray diffraction patterns selected from 18° to 21° in the red box of (a). (g) The corresponding discharge curve.

Table 1
Summary of the Rietveld Refinement Results.

Time (s)	NaV ₆ O ₁₅					V ₂ O ₅				
	Phase	a	b	c	Crystal system	Phase	a	b	c	Crystal system
0	Na _{1/3} V ₂ O ₅	10.039	3.605	15.355	Monoclinic	V ₂ O ₅	11.510	4.369	3.563	Orthorhombic
410	Li _{1/18} Na _{1/3} V ₂ O ₅	10.126	3.629	15.534	Monoclinic	V ₂ O ₅	11.510	4.369	3.563	Orthorhombic
1665	Li _{1/18} Na _{1/3} V ₂ O ₅	10.126	3.629	15.534	Monoclinic	Li _{1/2} V ₂ O ₅	10.814	3.772	14.310	Monoclinic
2500	Li _{1/6} Na _{1/3} V ₂ O ₅	10.287	3.666	15.534	Monoclinic	Li _{1/2} V ₂ O ₅	10.814	3.772	14.310	Monoclinic
3745	Li _{1/6} Na _{1/3} V ₂ O ₅	10.287	3.666	15.534	Monoclinic	Li _{1/2} V ₂ O ₅	9.898	3.573	10.478	Orthorhombic
5000	Li _{1/3} Na _{1/3} V ₂ O ₅	10.543	4.517	15.415	Monoclinic	Li _{1/2} V ₂ O ₅	9.898	3.573	10.478	Orthorhombic
10,000	Li ₁ Na _{1/3} V ₂ O ₅	15.201	10.00	20.776	Monoclinic	Li _{1/2} V ₂ O ₅	9.898	3.573	10.478	Orthorhombic

provides a specific bottom-up approach toward hierarchical heterostructures and can also be extended to other systems. Moreover, the synergistic effect between the branched vanadate (NaV₆O₁₅) and the backbone structure (V₂O₅) of 3D hierarchical heterostructure was clearly and detailed illustrated by *in situ* XRD. As concluded from this characterization, during the synergistic effect, the branched NaV₆O₁₅ effectively reduces the potential barrier and greatly buffers the impact of crystal-system transformations during the charge and discharge process; while the backbone V₂O₅ increases the charge/discharge capacity of 3D microspheres, inhibits the self-aggregation of branched NaV₆O₁₅ and maintains the stability of 3D hierarchical heterogeneous structure. As a consequence, 3D V₂O₅/NaV₆O₁₅ hierarchical heterogeneous microspheres exhibit excellent high-rate and long-life cycling performance. We believe these characterizations of synergistic effect demonstrate outstanding electrochemical performance of 3D hierarchical heterostructure and bring a new understanding of lithiation/delithiation, which is also beneficial to sodium-ion batteries, lithium-sulfur batteries and other systems.

Acknowledgments

This work was supported by the National Basic Research Program of China (2013CB934103), the National Key Research Program of China (2016YFA0202603), the National Natural Science Foundation of China (51521001, 51302203 and 51272197), the National Natural Science Fund for Distinguished Young Scholars (51425204), the Hubei Province Natural Science Fund for Distinguished Young Scholars (2014CFA035), the Fundamental Research Funds for the Central Universities (WUT: 2013-ZD-7 and 2014-VII-007) and the Students Innovation and Entrepreneurship Training Program (2014-CL-A1-01 and 2015-CL-B1-23). We thank Prof. D. Y. Zhao of Fudan University and Prof. J. Liu of Pacific Northwest National Laboratory for useful discussions and assistance with the manuscript.

Appendix A. Supporting information

Supplementary data associated with this article can be found in the online version at <http://dx.doi.org/10.1016/j.nanoen.2016.06.057>.

References

- [1] P.Y. Chen, M.N. Hyger, D. Mackanic, N.D. Courchesne, J.F. Qi, M.T. Klug, A. M. Belcher, P.T. Hammond, *Adv. Mater.* 26 (2014) 5101–5107.
- [2] Y.J. Hwang, C.H. Wu, C. Hahn, H.E. Jeong, P.D. Yang, *Nano Lett.* 12 (2012) 1678–1682.
- [3] Y. Fang, G.F. Zheng, J.P. Yang, H.S. Tang, Y.F. Zhang, B. Kong, Y.Y. Lv, C.J. Xu, A. M. Asiri, J. Zi, F. Zhang, D.Y. Zhao, *Angew. Chem. Int. Ed.* 53 (2014) 5366–5370.
- [4] Y. Yang, Z.C. Zhang, P.P. Wang, J.C. Zhang, F. Nosheen, J. Zhuang, X. Wang, *Inorg. Chem.* 52 (2013) 9449–9455.
- [5] S.H. Ko, D. Lee, H.W. Kang, K.H. Nam, J.Y. Yeo, S.J. Hong, C.P. Grigoropoulos, H. J. Sung, *Nano Lett.* 11 (2011) 666–671.
- [6] Z.K. Zheng, W. Xie, Z.S. Lim, L. You, J.L. Wang, *Sci. Rep.* 4 (2014) 5721.
- [7] C.M.A. Parlett, K. Wilson, A.F. Lee, *Chem. Soc. Rev.* 42 (2013) 3876–3893.
- [8] Q.C. Liu, J.J. Xu, D. Xu, X.B. Zhang, *Nat. Commun.* 6 (2015) 7892.
- [9] Z.G. Yang, J.L. Zhang, M.C.W. Kintner-Meyer, X.C. Lu, D. Choi, J.P. Lemmon, J. Liu, *Chem. Rev.* 111.5 (2011) 3577–3613.
- [10] M.R. Lukatskaya, O. Mashtalir, C.E. Ren, Y. Dall'Agnesse, P. Rozier, P.L. Taberna, M. Naguib, P. Simon, M.W. Barsoum, Y. Gogotsi, *Science* 341 (2013) 1502.
- [11] H.G. Zhang, X.D. Yu, P.V. Braun, *Nat. Nanotechnol.* 6 (2011) 277–281.
- [12] J.H. Pikul, H.G. Zhang, J. Cho, P.V. Braun, W.P. King, *Nat. Commun.* 4 (2013) 1732.
- [13] K. Miszta, J.D. Graaf, G. Bertoni, D. Dorfs, R. Brescia, S. Marras, L. Ceseracciu, R. Cingolani, R.V. Rojji, M. Dijkstra, L. Manna, *Nat. Mater.* 10 (2011) 872–876.
- [14] L.Q. Mai, X.C. Tian, X. Xu, L. Chang, L. Xu, *Chem. Rev.* 114 (2014) 11828–11862.
- [15] W.W. Zhou, Y.Y. Tay, X.T. Jia, D.Y.Y. Wai, J. Jiang, H.H. Hoon, T. Yu, *Nanoscale* 4 (2012) 4459–4463.
- [16] L.Q. Mai, F. Yang, Y.L. Zhao, X. Xu, X. Lin, Y.Z. Luo, *Nat. Commun.* 2 (2011) 381.
- [17] K. Biswas, J.Q. He, I.D. Blum, C. Wu, T.P. Hogan, D.N. Seidman, V.P. Dravid, M. G. Kanatzidis, *Nature* 490 (2012) 414.
- [18] J.X. Wang, Q.B. Zhang, X.H. Li, B. Zhang, L.Q. Mai, K.L. Zhang, *Nano Energy* 12 (2015) 437–446.
- [19] Y.J. Cui, A. Abouimrane, J. Lu, T. Bolin, Y. Ren, W. Weng, C.J. Sun, V.A. Maroni, S. M. Heald, K. Amine, *J. Am. Chem. Soc.* 135 (2013) 8047–8056.
- [20] M.Y. Yan, G.B. Zhang, Q.L. Wei, X.C. Tian, K.N. Zhao, Q.Y. An, L. Zhou, Y.L. Zhao, C.J. Niu, W.H. Ren, L. He, L.Q. Mai, *Nano Energy* 22 (2016) 406–413.
- [21] X.Q. Yu, H.L. Pan, W. Wan, C. Ma, J.M. Bai, Q.P. Meng, S.N. Ehrlich, Y.S. Hu, X. Q. Yang, *Nano Lett.* 13 (2013) 4721–4727.
- [22] L. Croguennec, M.R. Palacin, *J. Am. Chem. Soc.* 137 (2015) 3140–3156.
- [23] K.W. Nam, S.M. Bak, E.Y. Hu, X.Q. Yu, Y.N. Zhou, X.J. Wang, L.J. Wu, Y.M. Zhu, K. Y. Chung, X.Q. Yang, *Adv. Funct. Mater.* 23 (2013) 1047–1063.
- [24] C. Villevieille, M. Ebner, J.L. Gómez-Cámer, F. Marone, P. Novák, V. Wood, *Adv. Mater.* 27 (2015) 1676–1681.
- [25] S. Muhammad, S. Lee, H. Kim, J. Yoon, D. Jang, J. Yoon, J.H. Park, W.S. Yoon, *J. Power Sources* 285 (2015) 156–160.
- [26] X.L. Ji, D.Y. Liu, D.G. Prendiville, Y.C. Zhang, X.N. Liu, G.D. Stucky, *Nano Today* 7.1 (2012) 10–20.
- [27] W.W. Xu, K.N. Zhao, C.J. Niu, L. Zhang, Z.Y. Cai, C.H. Han, L. He, T. Shen, M. Y. Yan, L.B. Qu, L.Q. Mai, *Nano Energy* 8 (2014) 196–204.
- [28] W.W. Zhou, C.W. Cheng, J.P. Liu, Y.Y. Tay, J. Jiang, X.T. Jia, J.X. Zhang, H. Gong, H. H. Hng, T. Yu, H.J. Fan, *Adv. Funct. Mater.* 21 (2011) 2439–2445.
- [29] W.D. Shi, S.Y. Song, H.J. Zhang, *Chem. Soc. Rev.* 42 (2013) 5714–5743.
- [30] C. Wu, J. Maier, Y. Yu, *Adv. Mater.* 28 (2016) 174–180.
- [31] Y.N. Xia, Y.J. Xiong, B. Lim, S.E. Skrabalak, *Angew. Chem. Int. Ed.* 48 (2009) 60–103.
- [32] Y.N. Xia, X.H. Xia, H.C. Peng, *J. Am. Chem. Soc.* 137 (2015) 7947–7966.
- [33] J.J. Wang, P. Liu, C.C. Seaton, K.M. Ryan, *J. Am. Chem. Soc.* 136 (2014) 7954–7960.
- [34] C. Li, X.P. Han, F.Y. Cheng, Y.X. Hu, C.C. Chen, J. Chen, *Nat. Commun.* 6 (2015) 7345.
- [35] H.Z. Zhang, J.F. Banfield, *CrystEngComm* 16 (2014) 1568–1578.
- [36] E. Allahyarov, K. Sandomirski, S.U. Egelhaaf, H. Löwen, *Nat. Commun.* 6 (2015) 7110.
- [37] P.D. Yang, *Nature* 482 (2012) 41.
- [38] C.J. Niu, J.S. Meng, X.P. Wang, C.H. Han, M.Y. Yan, K.N. Zhao, X.M. Xu, W.H. Ren, Y.L. Zhao, L. Xu, Q.J. Zhang, D.Y. Zhao, L.Q. Mai, *Nat. Commun.* 6 (2015) 7402.
- [39] L. Zhang, H.B. Wu, X.W. Lou, *J. Am. Chem. Soc.* 135 (2013) 10664–10672.
- [40] J. Park, J. Joo, S.G. Kwon, Y. Jiang, T. Hyeon, *Angew. Chem. Int. Ed.* 46 (2007) 4630–4660.
- [41] J. Ju, Y.M. Zheng, L. Jiang, *Acc. Chem. Res.* 47 (2014) 2342–2352.
- [42] C.J. Niu, J.S. Meng, C.H. Han, K.N. Zhao, M.Y. Yan, L.Q. Mai, *Nano Lett.* 14 (2014) 2873–2878.
- [43] J. Liu, H. Xia, D.F. Xue, L. Lu, *J. Am. Chem. Soc.* 131 (2009) 12086–12087.
- [44] S.Q. Wang, S.R. Li, Y. Sun, X.Y. Feng, C.H. Chen, *Energy Environ. Sci.* 4 (2011) 2854–2857.
- [45] Q. Liu, Z.F. Li, Y.D. Liu, H.Y. Zhang, Y. Ren, C.J. Sun, W.Q. Lu, Y. Zhou, L. Stanciu, E. A. Stach, J. Xie, *Nat. Commun.* 6 (2015).
- [46] G.Z. Yang, H.W. Song, G.W. Yang, M.M. Wu, C.X. Wang, *Nano Energy* 15 (2015) 281–292.
- [47] H. Xia, Q.Y. Xia, B.H. Lin, J.W. Zhu, J.K. Seo, Y.S. Meng, *Nano Energy* 22 (2016)

- 475–482.
- [48] R. Mukherjee, R. Krishnan, T.M. Lu, N. Koratkar, *Nano Energy* 1 (2012) 518–533.
- [49] F.F. Wu, S.L. Xiong, Y.T. Qian, S.H. Yu, *Angew. Chem. Int. Ed.* 54 (2015) 1–6.
- [50] R.L. Tang, Y. Li, N.N. Li, D.D. Han, H. Li, Y.S. Zhao, C.X. Gao, P.W. Zhu, X. Wang, *J. Phys. Chem. C* 118 (2014) 10560–10566.
- [51] H.M. Liu, Y.G. Wang, L. Li, K.X. Wang, E. Hosono, H.S. Zhou, *J. Mater. Chem.* 19 (2009) 7885–7891.
- [52] X.S. Liu, J. Liu, R.M. Qiao, Y. Yu, H. Li, L.M. Suo, Y.S. Hu, Y.D. Chuang, G.J. Shu, F. C. Chou, T.C. Weng, D. Nordlund, D. Sokaras, Y.J. Wang, H. Lin, B. Barbiellini, A. Bansil, X.Y. Song, Z. Liu, S.S. Yan, G. Liu, S. Qiao, T.J. Richardson, D. Prendergast, Z. Hussain, F.M. Groot, W.L. Yang, *J. Am. Chem. Soc.* 134 (2012) 13708–13715.
- [53] J. Su, X.X. Zou, G.D. Li, X. Wei, C. Yan, Y.N. Wang, J. Zhao, L.J. Zhou, J.S. Chen, *J. Phys. Chem. C* 115 (2011) 8064–8071.
- [54] Y. Zheng, T.F. Zhou, C.F. Zhang, H.K. Liu, Z.P. Guo, *Angew. Chem. Int. Ed.* 55 (2016) 3408–3413.
- [55] D.L. Wood, J. Tauc, *Phys. Rev. B* 5 (1972) 3144–3151.



Chaojiang Niu is currently working toward the Ph.D degree in Wuhan University of Technology since 2013 and the major is Materials Physics and Chemistry. His current research focuses on the nanomaterials for energy storage.



Xiong Liu is an undergraduate student in the Department of Materials Science of Engineering from Wuhan University of Technology since 2012. His current research focuses on involves nanomaterials for energy storage.



Jiashen Meng received his B.S. degree from Wuhan University of Technology in 2015. He is currently working toward the Ph.D degree in Wuhan University of Technology and his current research focuses on the energy storage materials and devices.



Lin Xu received his Ph.D degree cosupervised by Professors Liqiang Mai and Qingjie Zhang at Wuhan University of Technology and Professor Charles M. Lieber at Harvard University. He is currently a postdoctoral fellow at Nanyang Technological University in the group of Professor Xiongwen Lou. His research focuses on nanoenergy devices and nanobioelectronics.



Mengyu Yan received his B.S. degree in Material Chemistry from China University of Geosciences in 2012 and he is currently working toward the Ph.D degree in Material Science at Wuhan University of Technology. His current research is nanoenergy materials and devices.



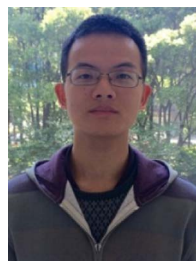
Xuanpeng Wang received his B.S. degree from Henan University of Urban Construction in 2013. He is currently working toward the Ph.D degree in Wuhan University of Technology and his current research focuses on the energy storage materials and devices.



Guobin Zhang received his B.S. degree from Inner Mongolia University of Science & Technology in 2014 and he is currently working toward the Master. Degree in Wuhan University of Technology. His current research focuses on *in situ* characterization.



Ziang Liu is an undergraduate student in the School of Materials Science and Engineering from Wuhan University of Technology since 2013. His current research involves nanoenergy materials and devices.



Xiaoming Xu received his B.S. degree in Material Science and Engineering from Wuhan University of Technology in 2014. He is currently working toward the Ph. D degree and his current research focuses on the energy storage materials and devices.



Liqiang Mai is Chair Professor of Materials Science and Engineering at Wuhan University of Technology (WUT), Distinguished Young Scholar of the National Science Fund of China, Executive Dean of International School of Materials Science and Engineering in WUT. He received Ph.D degree in WUT in 2004 and then worked as a postdoctoral researcher in Georgia Institute of

Technology in the group of Prof. ZL Wang from 2006 to 2007. He conducted nanowire based nanodevices and battery research as advanced research scholar in the group of Prof. CM Lieber in Harvard University from 2008 to 2011. He is mainly engaged in research field of nano energy materials and micro/nano devices.